POLITECNICO DI TORINO
Repository ISTITUZIONALE

Mechanical Behaviour of TiAl Spherical Particles Including Friction Effect

Original
Mechanical Behaviour of TiAl Spherical Particles Including Friction Effect / Cagliero, R.; Santoro, A.; Maizza, Giovanni. - ELETTRONICO. - (2010), pp. 1-11. (Intervento presentato al convegno COMSOL Conference 2010 Paris tenutosi a Paris nel November 17-19).

Availability:
This version is available at: 11583/2424064 since:

Publisher:
COMSOL

Published
DOI:

Terms of use:

This article is made available under terms and conditions as specified in the corresponding bibliographic description in the repository

Publisher copyright

(Article begins on next page)

24 April 2024

Mechanical Behaviour of TiAl Spherical Particles Including Friction Effect

R. Cagliero, A. Santoro, and G. Maizza*
Dipartimento di Scienza dei Materiali ed Ingegneria Chimica, Politecnico di Torino
*Corresponding author: C.so Duca degli Abruzzi 24, 10129, Torino, Italy, maizza@polito.it

Abstract: Powder metallurgy is a key technology for manufacturing advanced TiAl-based engineering components. Cold compaction is the primary step to produce green parts. However TiAl powders possess intrinsic poor room temperature ductility. On compaction, plastic deformation and cracking susceptibility of TiAl particles strongly depends on their micro-mechanical interaction. Hertz's law describes the elastic stress and deformation fields near the contact point of two contacting spheres and establishes a relationship between the applied compression force and displacements. However, this law only holds for static problems and does not include the effect of friction and plastic flow bounded in the vicinity of the contact point. To manage more realistic compaction problems of spherical particles more reliable elastoplastic models, involving large deformation and friction at particle interfaces, are required. The finite element method is proved to be an effective means in the quantitative prediction of stress and strain fields in nonlinear media provided that a reliable stress-strain curve and adequate contact conditions are defined. To optimize the overall cold compaction process of TiAl particles, a micro-mechanical elastoplastic model is developed, taking into account friction effects at particle interfaces. The results are provided in terms of force-displacement curves, stress-strain fields, contact area evolution and crack susceptibility in three designed aggregates.

Keywords: TiAl, spherical particles, elasto-plastic contact mechanics, friction, compaction.

1. Introduction

Intermetallic alloys, such as γ-TiAl, are candidate structural materials for high temperature applications [9] as they exhibit excellent mechanical specific properties, high melting point, and good creep and oxidation resistance. Conversely, their room temperature ductility is very low (about 0.5-1% fracture strain). This poses severe problems in manufacturing TiAl components since their workability is rather limited at room temperature.

Among the avaible manufacturing processes, powder metallurgy is in general suited for difficult-to-form and high melting point materials.

In particular, cold compaction is advantageous as it minimizes compositional changes during processing compared to thermal processes. However, it is difficult to apply to TiAl powder owing to their poor room temperature ductility.

Computer modeling can be helpful to preliminarily investigate the compactability features of TiAl powder.

This work presents an axial-symmetric micromechanical elastoplastic model applied to contacting particles in the presence of friction. The purpose is not the simulation of the real time dynamics of the compaction process, rather the prediction of the deformation and of the bearing capacity of TiAl particles before cracking or fracture. We have solved the mechanical problem as a multistage static analysis to simulate a transient problem [1].

Three different particle arrangement configurations (i.e. simulation cells) are investigated. The developed model is multi-contact and strongly non linear due to the involved large plastic deformations and friction at the contact boundaries.

2. The Cold Compaction Model

2.1 The geometry model

The configurations analyzed are shown in Fig. 1. They will be designated hereinafter as A-, B- and C-configurations.

A-configuration is the simplest and common to many sintering models. It consists of two equisized spheres in reciprocal contact. Axial-symmetry considerations lead to compute only

two quarters of the two spheres. *r* direction is the horizontal axis and *z* direction is the vertical axis.

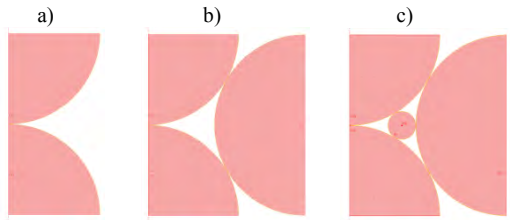

Figure 1. Multicontact configurations investigated.

B-configuration attempts to capture the effect of three particles in relative contacts. Keeping the cylindrical coordinate system for consistency to A-configuration, this configuration is modeled as two equisized particles surrounded by a toroidal ring.

C-configuration assumes a multicontact system to mimic a particle size distribution. It includes an additional smaller internal ring to previous B-configuration to fill the interparticle gap. Thus six contacts are present in total.

2.2 The bulk elastoplastic model

The fundamental theory of the employed elastoplastic model is described in detail in the Comsol Multiphysics User's guide [5]. In the following only an overview of it will be given.

In all configurations the particles are allowed to displace along *r* and *z* directions. The arrangements are assumed to be simultaneously loaded under displacement control along z direction. Thus, the particle cells are assumed to be uniaxially loaded. The contact pressures T_n and the friction traction vector T_t at each interface being unknown are calculated by Comsol.

The contacts between the spheres and the rings are assumed to behave elastoplastically undergoing large deformations. The stress-strain constitutive equations include other than the elastic and the plastic term also the initial contact pressure condition.

Since the isotropic hardening model is set, the yield surface would grow in size while its center remains at a fixed point. In the isotropic model the flow stress is written as:

$$\sigma_{yhard} = \sigma_{\exp}(\varepsilon_{eff}) - \sigma_y \tag{1}$$

where σ_y is yield stress and σ_{exp} is an experimental stress function. The latter can be an experimental uniaxial true stress-strain tension curve. The start of yielding is evaluated by the von Mises criterion.

The large deformations are modeled by the Green strain function over the undeformed geometry domain whereas the stresses are replaced by the second Piola-Kirchhoff stresses.

2.3 The contact model

The normal contact pressure T_n and the components of the friction traction vector T_t are taken as field variables.

In Comsol 3.5 the contact problem is managed by the "contact pairs" model. A master and a slave pair is defined for each contact interface. For A-configuration, the upper sphere is defined as a master and the lower sphere is defined as a slave. The gap distance *g* between the slave and the master boundaries is computed to define the penalized contact pressure at the slave boundary.

This pressure is defined as:

$$T_{np} = \begin{cases} T_n - p_n g & if \quad g \le 0 \\ T_n e^{\left(\frac{p_n g}{T_n}\right)} & otherwhise \end{cases} \tag{2}$$

where p_n is the normal penalty factor. The last value is calculated iteratively according to:

$$p_{\max} = \frac{E}{h_{\min}} \cdot \min(10^{-3} \cdot 5^{auglagiter}, 1) \tag{3}$$

in which E is the slave Young's modulus, $h_{\min}$ is the smallest mesh size at the slave boundary and $auglagiter$ is the iteration number in the augmented Lagrangian solver.

The penalized friction traction T_{tp} is defined as:

$$T_{tp} = \min\left(\frac{T_{tcrit}}{|T_{ttrial}|}, 1\right) T_{ttrial} \tag{4}$$

where:

$$T_{ttrial} = T_t - p_t map(F)(x^m - x^m_{old}) \quad (5)$$

$$x^m = map(x) \quad (6)$$

and p_t is the friction traction penalty factor calculated with the same equation of the normal penalty factor, x is the space coordinates, x_{old} is the value of x^m in the last time step, F is the deformation gradient matrix and $map(F)$ is the value of F computed at the corresponding master point. Analogously, $map(x)$ has the same meaning of map(F) with the sole difference that it refers to x value. Therefore, the term $map(F)(x^m - x^m_{old})$ can be viewed as the slip vector. The term T_{tcrit} is defined as:

$$T_{tcrit} = \min(\mu T_{np} + cohe, T_{t\max}) \quad (7)$$

where T_{tmax} is the maximum friction traction, μ is the static friction coefficient and *cohe* is the cohesion sliding resistance, which is defined as the friction force at zero contact pressure.

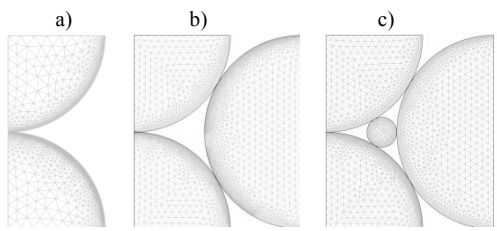

Figure 2. Initial mesh: a) A-configuration; b) B-configuration; c) C-configuration.

2.4 Boundary conditions

The boundary conditions for the three configurations are illustrated below.

A-configuration:
- symmetry (i.e. zero normal displacements) at the horizontal midplane of the lower sphere;
- symmetry at the vertical symmetry plane;
- displacement control by kinematic constraint at the horizontal midplane of the upper sphere;
- free at all remaining boundaries.

The kinematic constraint is specified by an user defined equation as a function of a displacement parameter (*displ_param*). The approach distance between the two sphere is given by:

$$appr_dist = 2 \cdot R - displ_scale \cdot displ_param \quad (8)$$

where R is the sphere radius. The *displ_scale* and the *displ_param* are defined by the user as explained below.
B-configuration:
The two spheres take the same boundary conditions as illustrated for A-configuration.

At the vertical midplane of the toroidal ring we assume zero displacement along the axial (z) and radial (r) directions.
The interface boundary is considered to be free.

C-configuration:
For the two spheres and the large toroidal ring the boundary conditions are the same as for B-configuration.
The smaller toroidal ring is assumed to be free.

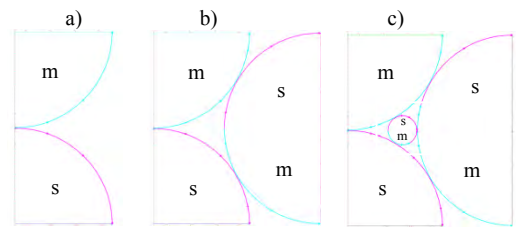

Figure 3. Boundary conditions and contact pairs (m = master, s = slave).

3. Model implementation and solution strategy

The micromechanical compaction model is solved using the static elastoplastic analysis with the parametric solver of the Structural Mechanics Module of Comsol Multiphysics 3.5 [5, 6, 7].
This choice is imposed by the inability of this module to solve real time dependent contact problems in combination with the elastoplastic solver.

The elastoplastic model is based on an experimental work hardening law for the examined material. This implies that the multistage procedure takes into account the non linear function of materials properties with strain.

The compression behaviour of the designed particle/ring systems is solved under displacement control mode. This is implemented by defining a suitable displacement parameter (*displ_param*) at the top sphere midplane boundary. This enters in the model as a boundary condition by which we control the degree of the relative approach of the spheres and the rings.

3.1 Bulk

The experimental uniaxial true stress-true strain curve for the investigated material (TiAl) is reported in Fig. 4. This curve, which is interpolated in Comsol by cubic spline, is used to determine $\sigma_{\exp}$ (eq. 1).

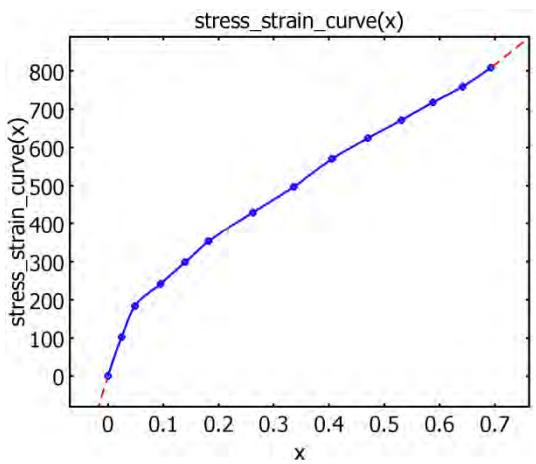

Figure 4. Experimental uniaxial true stress-true strain tension curve of TiAl.

Form Fig 4 the Young's modulus and the yield stress (i.e. 168 GPa and 275.8 MPa respectively) can be extracted. The Poisson's ratio is assumed to be equal to 0.263.
The diameter of the particles is 0.150 mm. The diameter of the two contacting rings is 0.150 and 0.023 mm.

3.2 Solution strategy and parameter setting

The solution of the overall elastoplastic/contact problem is found iteratively by a user-defined multistage procedure of composed intermediate steady-state elastoplastic solutions. This procedure is controlled by the displacement parameter (*displ_param*) using equal increments. Each non-linear elastoplastic stage is solved using the damped Newton method. The direct UMFPACK is selected to solve the algebraic linear system. Within each stage the boundary conditions and the material properties are assumed to be constant [3,9].

The *displ_scale* parameter is set equal to the radius of the sphere (0.075 mm) and the displacement parameter values (*displ_param*) are always incremented of 0.001.

The contact problem is solved by the *augmented Lagrangian* method where the contact pressure T_n and the friction tractions T_{tx} and T_{ty} are the augmented variables. This method is run with the *lumped solver* setting 25 as the maximum number of iterations and 10 MPa as tolerance. The *lumped solver* attemps to minimize possible undershoots in the contact regions.

The geometric configuration of the previous stage is entered as starting configuration in the next stage. Accordingly, at each stage the current contact force is updated [1].

If convergence is difficult, the parametric solver reduces the size of the parameter step. However, the maximum number of iterations per stage is fixed to 25. If the solve fails after 25 iterations, the previous stage is taken as a final solution. Among other information, the final solution contains the maximum tensile deformation of particles before cracking or fracture. This condition occurs when the related tensile stress is greater than the fracture stress of the material.

To prevent the solvers' failure, the initial contact between the spheres and the rings must be sufficiently tight. This is ensured by imposing a small value for the initial contact pressure and the initial friction force in z-direction. To this purpose an initial pressure and friction force of 10 MPa is assumed resulting in a very small deformation in the initial contact configuration. In this manner, the solver is able to detect one contact point in the initial stage. The subsequent contact points are found by the direct search method. The absolute search distance is set to 10^{-4} mm which is of the same order of magnitude of the largest mesh element in the contact pair.

In all configuration cases the cohesion sliding resistance (*cohe*), the maximum friction traction (T_{tmax}) and the static friction coefficient (μ) are set to 0 MPa, infinite and 0.66 respectively [8].

Only for the A-configuration case, the initial value of the friction force in r-direction is assumed to be null.

The tolerances for the augmented Lagrangian components are set to 10 MPa. Their manual scaling values are equal to 10^3. For the *z* and *r*-displacements, the manual scaling is 10^{-2}. The relative tolerance is always set to 10^{-3}.

The Rayleigh damping parameters, α_{dM} and β_{dK}, are equal to 1 s^{-1} and 0.001 s respectively.

3.3 The domain discretization

All configurations are discretized with linear triangular finite elements.

As for the initial free mesh parameters, a *normal* predefined mesh size is selected at global scale. The adaptive mesh generation helps identify the regions that require higher resolution. The error estimator employs the functional norm which applies to the global *z* displacement (w).

As element selection mode the *rough global minimum* method is selected. In this method the elements having the largest error are refined such that the total number of refined elements is limited to 70% increase. The chosen refinement algorithm is the *meshinit* method.

As far as the contact interfaces, the mesh is finer at the slave boundaries than at the master boundaries. Specifically, for A-configuration, the maximum element size at the contact boundaries of the upper sphere (master) is set to $7.5*10^{-4}$ mm and that at the contact boundaries of the lower sphere (slave) is set to $2.5*10^{-4}$ mm. The element growth rate is set to 1.3 in the upper sphere and 1.25 in the lower sphere. For the A-configuration, the initial mesh consists of 8,732 elements and 43,411 degrees of freedom.

For B-configuration, the maximum element size is $1.5\cdot10^{-3}$ mm for the upper sphere (master) and $5\cdot10^{-4}$ mm for the lower sphere (slave). The boundary of the ring is divided into two zones thus identifying the master and the slave for each contact. The maximum element size is $5\cdot10^{-4}$ mm for the lower boundary zone and $1.5\cdot10^{-3}$ mm for the upper boundary zone. The initial number of elements and degrees of freedom are 8,468 and 42,470 respectively.

C-configuration comprises B-configuration with a new inner ring. The maximum element size of the inner ring is $1\cdot10^{-3}$ mm. The initial mesh consists of 7,473 elements and 37,079 degrees of freedom.

4. Results and Discussion

4.1 A-configuration

Figures 5-6 show the deformed shape and the von Mises stress in the two spheres as calculated by the multistage elastoplastic/contact procedure under displacement control mode. Each solution corresponds to a specified displacement parameter or approaching distance between the two spheres. For better insight, the approaching distance is indicated in each figure rather than the *displ_param*. However, the latter can be readily calculated using eq. (8). As can be seen, the stress field is non symmetric due to the non symmetric loading condition. The stress field progressively extends in the bulk of the two spheres with decreasing their approaching distance (*appr_dist*). The larger effective stress value is always concentrated near the end of the contact area (or contact tip) and is equal to 927 MPa for an approaching distance of 0.138 mm.

In the A-configuration, the convergence is difficult because the spheres are equisized and have the same material properties.

According to the contact theory, a contact problem solution will converge more rapidly to a solution if the master is designed to be stiffer than the slave.

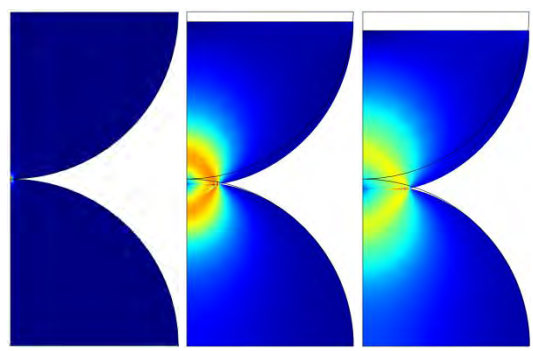

Figure 5. A-configuration: von Mises stress at different *appr_dist* values: a) 0 mm (max stress = 3 MPa); b) 0.145 mm (max stress = 357 MPa); c) 0.141 mm (max stress = 526 MPa).

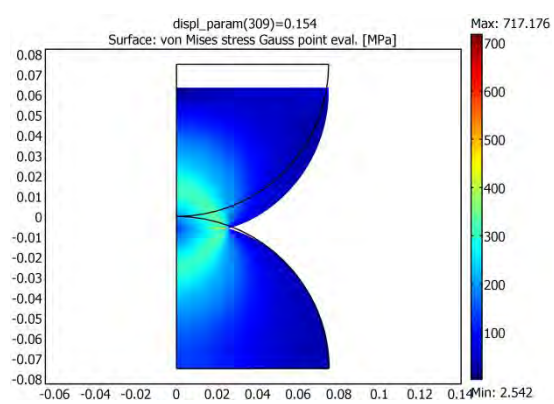

Figure 6. A-configuration: von Mises stress at *appr_dist*=0.138 mm (max stress = 927 MPa).

As the system is compressed under a displacement control mode, we can calculate the equivalent overall force applied at the top boundary (constrained displacement) of the upper sphere. This is accomplished by adding the nodal reaction forces in the z-direction.

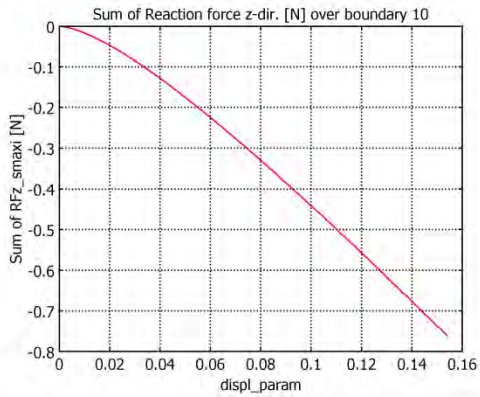

Figure 9. A-configuration: force exerted over the lower sphere vs displacement parameter (*displ_param* = 0.154 corresponds to *appr_dist* =0.138 mm).

A useful output is the total displacement which is defined as $\sqrt{(uor*r)^2+w^2}$ and shown in Fig. 10 (a) for the minimum approaching distance of 0.138 mm. As can be observed, the upper sphere undergoes larger displacements compared to the lower sphere. In particular, the total displacement of the upper horizontal boundary is larger than that of the contact boundary due to bulk elastoplastic deformation of the upper sphere.

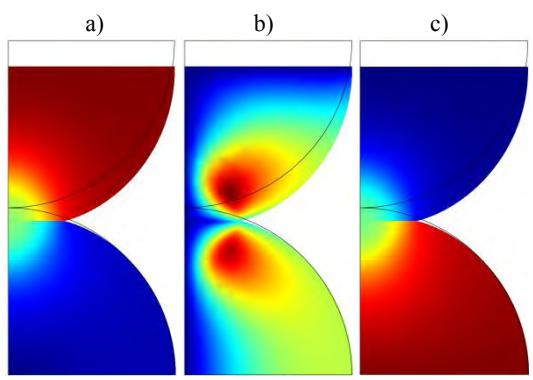

Figure 10. A-configuration: a) total displacement for *appr_dist* =0.138 mm (total max displacement = 0.0115 mm). b) r-displacement for *appr_dist* =0.138 mm (max r-displacement = $9\cdot10^{-4}$ mm). c) z-displacement for *appr_dist* =0.138 mm (max z-displacement = 0.0115 mm).

Figure 9 shows the magnitude of this force against the approaching distance. Note that this force is equal to the integral of the contact pressure over the contact area.

Analogously, Figs. 10 (b) and 10 (c) show the radial displacement (*uaxi* = *uor* * *r*) and the axial displacements (*w*), respectively. The radial displacements in the two spheres are balanced at the contact interface. Their values depend on the contact friction forces. The larger values are attained nearby the end of the contact area. However, the axial displacements (Fig. 10 (c)) are not balanced as they reflect the total displacement and the pure radial displacements are negligible.

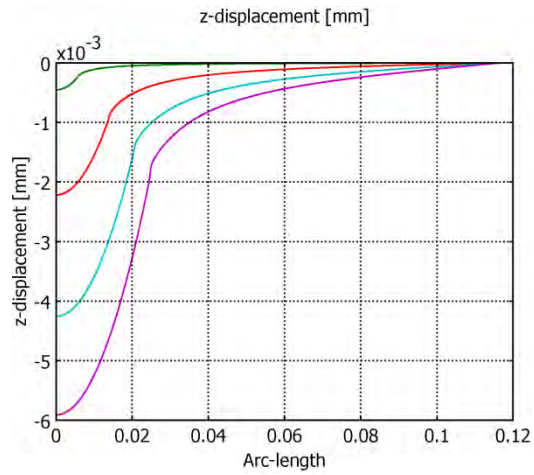

Figure 11. A-configuration: z-displacement vs slave boundary arc length for *appr_dist* =0.1491 (top curve), 0.1456, 0.1416 and 0.1384 mm (bottom curve).

Figure 11 shows the change of the axial displacement versus the arc length of the slave boundary for various approaching distances. The initial contact point experiences the greatest displacement. This figure suggests that there is no indication of pile-up which would arise if the displacements were positive.

The bottom curve also describes the displacement of the initial contact point. It reaches a value of -0.0059 mm, at the smallest approaching distance of 0.1384 mm. Such displacement equals the shrinkage along the z-axis of the lower particle. The shrinkage of the upper sphere is obtained by the maximum z-displacement at the upper sphere (i.e. 0.0634 mm) minus the shrinkage of the lower sphere (0.0059 mm), that is 0.057 mm.

Figure 12 shows the radial displacement versus the slave boundary arc length for various approaching distances. This figure highlights the presence of positive and small initial negative displacements. All curves tend to attain an asymptotical value. The undershoots means negative displacements near the contact interface. They only appear in the first curve related to 0.1491 mm approaching distance.

Practical considerations can also be made knowing the extension of the contact area is known in function of the approaching distance. However, as the radius of the contact area is not directly computed by COMSOL, it has to be computed using the predicted fields. Figure 13 is helpful with this regard. It shows the behaviour of the contact pressure with decreasing approaching distance. As can be seen the contact pressure curves are not smooth because of the strongly non linear elastoplastic behaviour of the contact problem. Nevertheless, they can be used to deduce the radius of the contact area. By definition, this is identified by a null contact pressure [5]. These values can be directly read as intersection points along the horizontal axis.

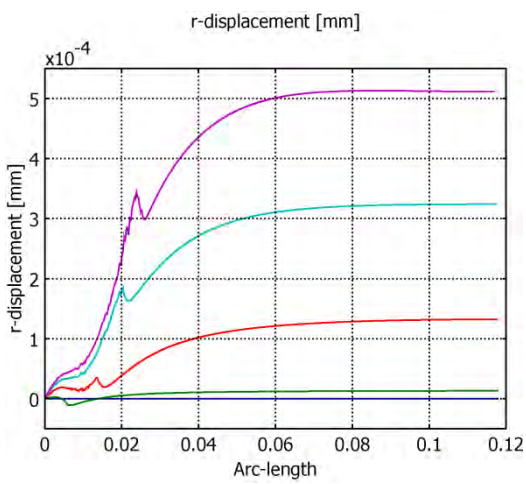

Figure 12. A-configuration: r-displacement vs slave boundary arc length for *appr_dist* =0.1491 (bottom curve), 0.1456, 0.1416 and 0.1384 mm (top curve).

In the case of the last displacement parameter, the contact pressure curve is noisy thereby making more complicated the identification of the intersection point. A magnification of the curve around the intersection areas suggests that the last intersection point is the one of interest. The maximum value of the contact radius is 0.0255 mm when the minimum approaching distance is 0.1384 mm. The contact radii are clear for lower displacement parameters, whereas they are less clear for larger displacement parameters. Incidentally, figures 12 and 13 appear to be related as the occurrence of the undershoot corresponds to the contact radius for each approaching distance (or displacement parameter).

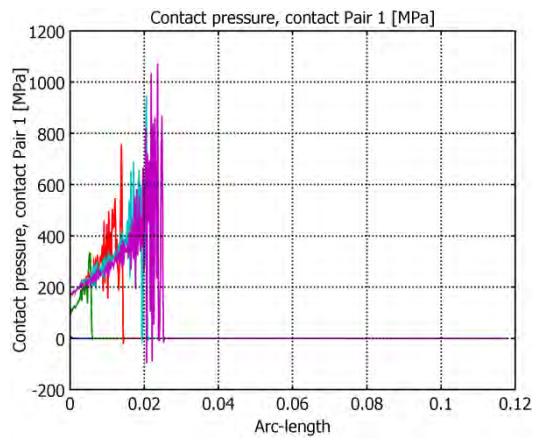

Figure 13. A-configuration: contact pressure vs slave boundary arc length for *appr_dist* =0.149, 0.1456, 0.1416 and 0.1384 mm.

To calculate the contact radii a logical expression is defined over the slave boundary such that it is equal to 1 in the absence of contact and zero in the presence of contact (i.e. non-zero contact pressure). Assuming a round contact area, its behaviour with the approaching distance is shown in Fig. 14.

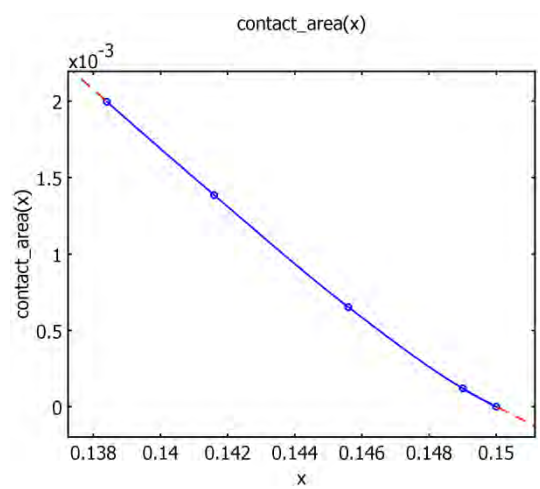

Figure 14. A-configuration: contact area vs approaching distance.

Friction forces are larger along the r-axis than the z-axis. It is shown that the friction coefficient of TiAl depends primarily on the aluminum content [8] since the dry sliding friction can be related to adhesion, ploughing and asperity deformation. If aluminum content is high, asperity deformation is more significant than adhesion. During compaction, intense localized heat can be generated due to friction forces, which lowers the strength of the contact surfaces and, in turn, lowers the friction coefficient. An increase in the static friction coefficient will result in a more difficult convergence of the contact model.

For validation purposes, A-configuration is also numerically solved in the case of the hertzian contact between two TiAl isotropic spheres. Hertz's problem assumes a purely elastic contact involving no friction and a contact area significantly smaller than both the size of the body and the radius of the surface curvature. Although this idealized contact situation hardly occurs in real practice, a closed-form solution allows for a direct comparison between the elastic and the elastoplastic response of the given material. Specifically, assuming a Poisson's ratio of 0.3, the analytical solution indicates a maximum value of $|\sigma_z-\sigma_r|$ at $0.48 \cdot a$ depth where a is the contact radius.

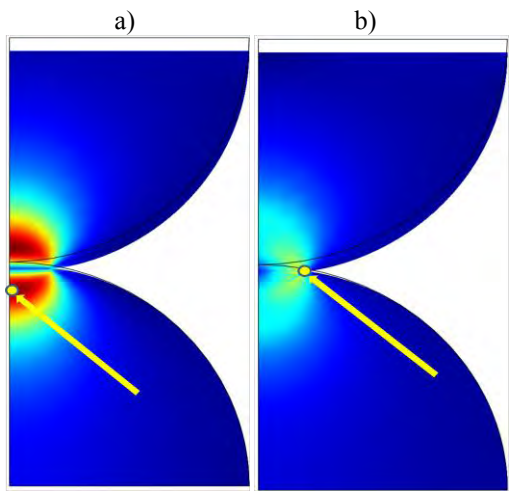

Figure 15. A-configuration: $|\sigma_z-\sigma_r|$ distributions for appr_dist =0.145 mm for a) elastic and b) elastoplastic behaviour of TiAl. The arrow indicates the maximum values.

In the elastoplastic problem involving friction the maximum value of $|\sigma_z-\sigma_r|$ is localized at the end of the contact area while in the elastic problem it is localized at $0.48 \cdot a$ depth (=0.0064 mm).

4.2 B-configuration

The number of active contacts in B-configuration is three. The lateral ring suffers a larger stress at the upper contact compared to the lower contact, due to non symmetric loading.

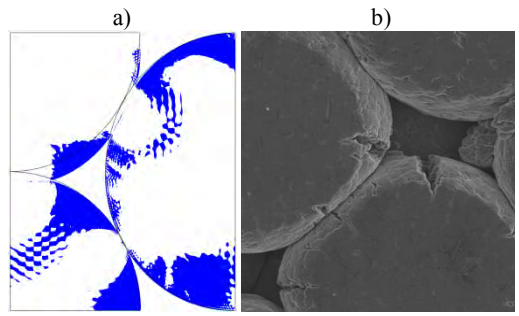

Figure 16. B-configuration: a) first principal tensile stresses for *appr_dist* =0.141 mm; b) SEM micrograph of the real TiAl particles after uniaxial compression taken from the nearby die wall (1600 X).

The major stress is still found at the sphere-sphere contact.

While the three contacts are in compression, the regions between them are slightly tensile. Figure 16 (a) highlights these tensile regions (blue regions).

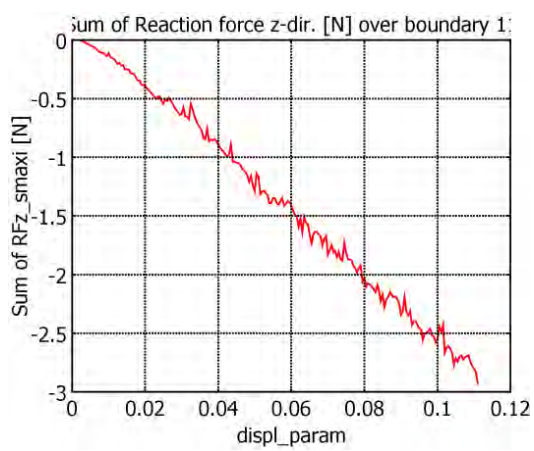

Figure 17. B-configuration: force exerted over the system vs displacement parameter (*displ_param* =0.111 corresponds to *appr_dist* =0.141 mm).

These regions are highly susceptible of superficial cracking provided the local stress surpass the tensile fracture stress of the material. Figure 16 (b) clearly stresses this event.
The maximum principal stress calculated inside the blue regions is equal to 1,752 MPa which is higher than the tensile fracture stress of TiAl (410 MPa). Notice that in Fig. 16 (b), minor cracks develop in the compressive regions (white regions) probably owing to the occurrence of high friction tensile stresses.
Comparing Fig.17 and Fig.9 we notice that the compressive force exerting the same approaching distance of 0.141 mm (or displacement parameter of 0.111) is lower in A- than in B-configuration (-0.45 vs - 2.90 N).
Indeed, an increase in the number of contacts leads to an increase of the compressing force at constant approaching distance.

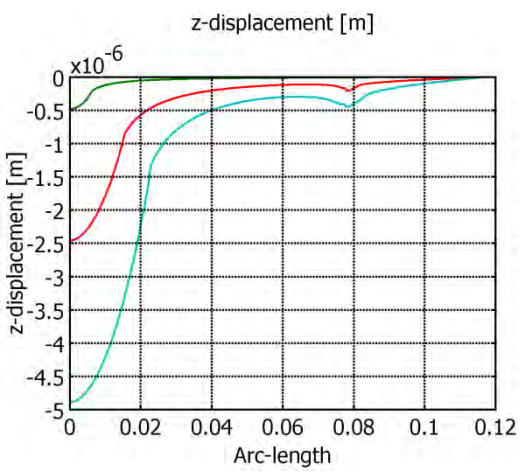

Figure 18. B-configuration: z-displacement vs slave boundary arc length for *appr_dist* =0.1491 (top curve), 0.1456, 0.1416 mm (bottom curve).

Notice that both the reactions and the friction forces here are overestimated compared to a more realistic aggregate of spherical particles due to the presence of the ring. This forces increase may cause a fragmentation of small particles during the first stages of cold compaction (i.e. *geometric hardening* [10]).

Fig. 18 reports the z-displacements vs arc length along the slave sphere boundary for various displacement parameters. The negative portions (compressive) are related to the two contact zones.

For the maximum calculated displacement parameter, the initial contact point between the spheres moves of 0.00488 mm downward whereas the overall shrinkage of the upper sphere is 0.00345 mm. The change of the radius of the contact area vs the approaching distance can be estimated as before from Fig.19 and therefore omitted.

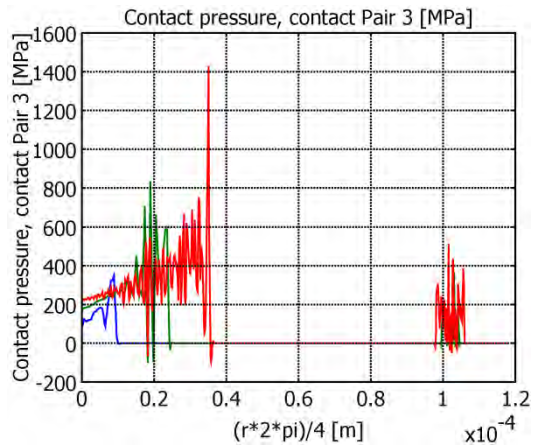

Figure 19. B-configuration: contact pressure vs length of the slave contact boundary for various approaching distances (0.149, 0.145, 0.141 mm).

For the minimum approaching distance, the radius of the sphere-sphere contact area is 0.0223 mm to be compared with the radius of the lower sphere-ring contact area which is 0.00545 mm.

Comparative considerations on A- and B-configurations with specific reference to fracture susceptibility will be discussed jointly with C-configuration.

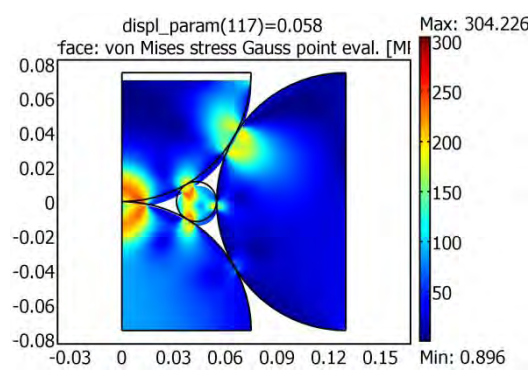

Figure 20. C-configuration: von Mises stress at *appr_dist* =0.145 mm (max stress = 379 MPa);

4.3 C-configuration

C-configuration is intended to explore the compaction ability of a more complex particle

system. To take computational advantages from the axial-symmetry, the lateral particles are replaced by two toroidal rings. Figure 20 depicts the von Mises stress distribution.

The small ring undergoes larger contact compressive stress compared to that at other contact interfaces. This highlights the dominant tendency of the small ring to fracture due to its relatively lower bearing resistance.

Figure 21 (a) shows the tensile stress regions where fracture is more likely to occur. Figure 21 (b) shows a real aggregate of TiAl particles taken nearby the die wall after uniaxial compaction.

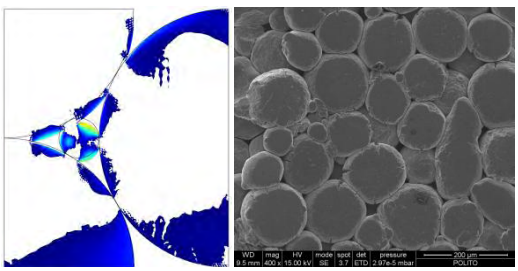

Figure 21. C-configuration: a) first principal tensile stress for *appr_dist* =0.145 mm; b) SEM micrograph of a real TiAl powder after uniaxial compression.

As can be seen, the small particles suffers higher tensile stresses and thus are prone to cracking.

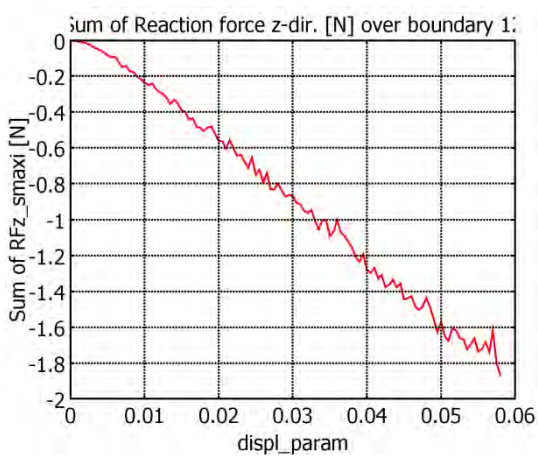

Figure 22. C-configuration: force to deform the spheres and the rings vs displacement parameter. The displ_param =0.058 corresponds to *appr_dist* = 0.145 mm.

The force required to deform the spheres and the rings vs displacement parameter is presented in Fig. 22. Comparing Fig.22 with Fig.9 and Fig.17, the compressive force exerting the same approaching distance of 0.145 mm is larger in C-configuration (-1.85 N) than in A- and B-configurations due to the increase in the number of contacts.

Figure 23 shows the z-displacements vs arc length along the slave sphere boundary for four displacement parameter values.

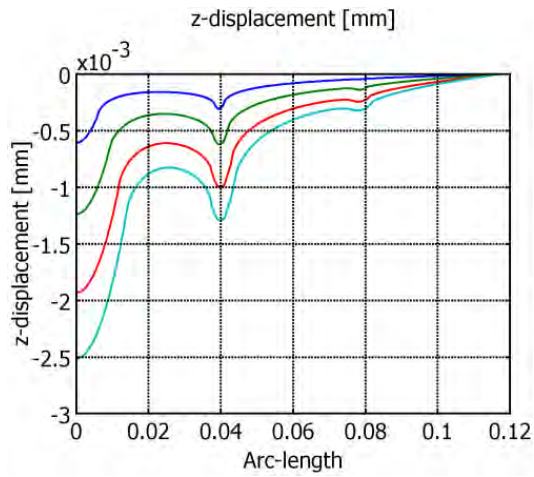

Figure 23. C-configuration: z-displacement vs slave boundary arc length for various approaching distances 0.1489 (top curve), 0.1478, 0.1466 and 0.1456 mm (bottom curve).

The local minima (compressive state) are related to the three contact zones.

For the lowest calculated approaching distance (0.145 mm), the initial contact point between the spheres moves of 0.00251 mm downward whereas the overall shrinkage of the upper sphere is 0.00184 mm.

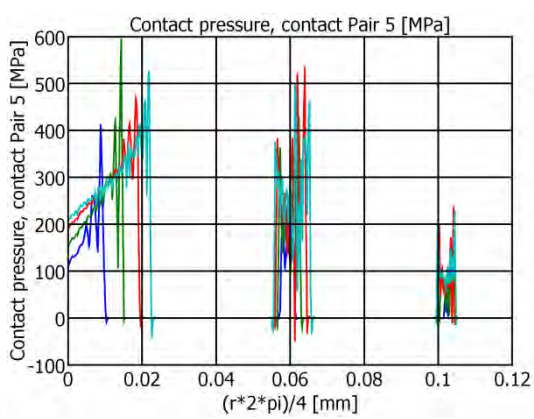

Figure 24. C-configuration: contact pressure vs length of the slave contact boundary for various approaching distances 0.1489, 0.1478, 0.1466 and 0.1456 mm.

Analogously to before, the change of the contact area vs the approaching distance can be estimated from figure 24. For the lowest approaching distance, the radius of the sphere-sphere contact area is 0.0144 mm to be compared with that of the sphere-small ring of 0.00375 mm and that of the sphere-larger ring of 0.0116 mm.
From the compaction viewpoint, the presence of numerous particles gives rise to a multitude of contacts which tend to equi-distribute the maximum equivalent stress in the aggregate. Work hardening tends to be more uniform in aggregates with larger number of particles compared to aggregate with a lower number of particles. This occurs when the aggregate consists of particles with quite different size distribution. In addition, a uniform work hardening ensures the creation of new deformation paths which may help densification. This situation is fulfilled by C-configuration, as it shows the larger number of contacts.

5. Conclusions

A micromechanical elastoplastic model mdoel has been developed to study the multi-axial compression behaviour of TiAl in three particle aggregate systems. The model taken into account friction effects. The stress-strain fields and the extension of the contact area have been analyzed with increasing the number of contacts. The contact regions are compressive while the adjacent regions are tensile. The presence of a large number of contacts ensures a more uniform distribution of stress-strain and work hardening for the same approaching distance. Among the three configurations C-configuration has the larger number of contacts thereby exhibits more uniform work hardening. The critical regions prone to cracking are located between the compression regions. Cracking events occur when the local tensile stress is larger than the fracture tensile stress of the material. The study contributes to elucidate fragmentation mechanisms of particles undergoing elastoplastic behaviour in presence of numerous concomitant contacts and friction. The developed model can be used to estimate the geometric hardening during cold compaction of a wide range of particle materials behaving elastoplasically.

6. References

1. Loc Vu-Quoc, Xiang Zhang, Lee Lesburg, Normal and tangential force-displacement relations for frictional elasto-plastic contact of spheres, *Journal of Solids and Structures*, **38**, 6455-6489 (2001).
2. N.P. Padture, *Encyclopedia of Materials: Science and Technology*, 3750-3752. Elsevier, N.Y. (2001).
3. K.L. Johnson, *Contact Mechanics*, chaps. 4-6, 10. Cambridge University Press, N.Y. (1985).
4. Loc Vu-Quoc, Xiang Zhang, An elastoplastic contact force–displacement model in the normal direction: displacement-driven version, *Proc. R. Soc. Lond.,* **A 455**, 4013–4044 (1999).
5. Comsol Multiphysics, *Structural Mechanics Module*, User's Guide, Vers. 3.5 (2008).
6. Comsol Multiphysics, *Structural Mechanics Module*, Model Library, Vers. 3.5 (2008).
7. Comsol Multiphysics, *Structural Mechanics Module*, Reference Guide, Vers. 3.5 (2008).
8. C.L. Chu, S.K. Wu, A study on the dry uni-directional sliding behaviour of titanium aluminides, *Scripta Metallurgica et Materialia*, **33**(1), 139-143 (1995).
9. E. A. Loria, Quo vadis gamma titanium aluminide, *Intermetallics* **9**(12), 997-1001 (2001).
10. E. Arzt, H. Fischmeister, Fundamental aspects of the compaction of metal powders, *Mémoires Scientifiques Revue Méallurgie*, 573-580 (1979).

7. Acknowledgements

The authors wish to express their sincere appreciation to Regione Piemonte (local government) – Direzione Regionale alle Attività Produttive - for funding the Green Engine for Air Traffic 2020 (Great 2020 - Ecoprolab) research project of Bando Regionale 24/12/2007 – Misura Ri.7 – Asse 1 "Ricerca e Innovazione" – (LR 34/2004) which has allowed the development of the present research work. Also, the AVIO S.P.A. group (Rivalta – TO) and the AvioProp s.r.l. (NO) are deeply acknowledged for providing the mechanical data.